The role of cohesive properties on intergranular crack propagation in brittle polycrystals

Shabir, Z.; Van der Giessen, E.; Duarte, C. A.; Simone, A.

Published in:
Modelling and Simulation in Materials Science and Engineering

DOI:
10.1088/0965-0393/19/3/035006

Publication date:
2011

Modelling Simul. Mater. Sci. Eng. **19** (2011) 035006 (21pp) doi:10.1088/0965-0393/19/3/035006

The role of cohesive properties on intergranular crack propagation in brittle polycrystals

Z Shabir[1], E Van der Giessen[2], C A Duarte[3] and A Simone[1]

[1] Faculty of Civil Engineering and Geosciences, Delft University of Technology, PO Box 5048, 2600 GA Delft, The Netherlands
[2] Zernike Institute for Advanced Materials, University of Groningen, Nyenborgh 4, 9747 AG Groningen, The Netherlands
[3] Department of Civil and Environmental Engineering, University of Illinois at Urbana-Champaign, 2122 Newmark Laboratory MC 250, 205 North Mathews Av., Urbana, IL 61801, USA

E-mail: a.simone@tudelft.nl

Received 2 October 2010, in final form 22 February 2011
Published 16 March 2011
Online at stacks.iop.org/MSMSE/19/035006

Abstract
We analyze intergranular brittle cracking of polycrystalline aggregates by means of a generalized finite element method for polycrystals with cohesive grain boundaries and linear elastic grains. Many random realizations of a polycrystalline topology are considered and it is shown that the resulting crack paths are insensitive to key cohesive law parameters such as maximum cohesive strength and critical fracture energy. Normal and tangential contributions to the dissipated energy are thoroughly investigated with respect to mesh refinement, cohesive law parameters and randomness of the underlying polycrystalline microstructure.

(Some figures in this article are in colour only in the electronic version)

1. Introduction

Cracking of a polycrystalline material depends on the loading conditions, the microstructure, and the mechanical behavior of grains and grain boundaries. In materials such as ceramics, where the grains are hard and strong, fracture occurs by crack growth along the grain boundaries. This kind of brittle intergranular fracture is often modeled by way of the finite element method (FEM) using the cohesive zone concept, where the response of the grain boundaries ahead of the crack tip is lumped into discrete lines [17, 18, 28, 36, 38, 39, 41]. Although appealing from a physical point of view, cohesive zone models come with numerical issues. They are essentially connected to cohesive zone models containing a small length scale: the so-called cohesive length. This length scale is a function of the cohesive properties—strength and fracture energy—and grain elastic constants. In order to obtain reliable numerical

results, the spatial discretization must be able to resolve well such length scales. Consequently, grain boundaries with different parameters require different discretizations, complicating the task of performing automatic parameter studies.

The FEM, in combination with cohesive zone models, guarantees a high quality in the characterization of local and global behavior of mesoscopic polycrystalline aggregates in terms, for instance, of stress–strain curves, stress fields and crack path, but the generation of acceptable finite element meshes may be difficult and requires user intervention. This can be a major issue when a large number of polycrystal geometries are considered. Other numerical procedures have been developed recently to describe discrete cracking in polycrystals. The boundary element method [29] can deliver solutions that are comparable to that obtained with the FEM at a high computational cost. On the other hand, approaches based on lattice or spring models [8, 13], the fuse model [35], and the grain element model [24] are based on simplified assumptions that guarantee cheaper computations at the expense, in some cases, of the quality of the numerical results. Probabilistic models for polycrystalline microstructures [2, 6] are even less costly, but can only deliver crack paths.

In this contribution, at variance with previous studies on brittle cracking of polycrystalline aggregates, we make use of a generalized finite element method (GFEM) for polycrystals [30]. This method is based on the partition of unity property of finite element shape functions [3, 9, 19, 21] and considerably simplifies the process of automatic mesh generation and refinement, as briefly illustrated in sections 2.1 and 2.3.

We perform an extensive study of many aspects of crack propagation in brittle polycrystals. With the constraint on the mesh size as defined in section 3.1, we demonstrate in sections 3.2–3.4 that the crack path depends only on the polycrystalline microstructure topology. An interesting consequence of this result is that reliable crack paths can be obtained at a relatively low computational cost for truly brittle polycrystals. Finally, the relation between polycrystalline microstructure and cohesive law parameters and their role on energy dissipation are discussed in sections 3.5 and 4.

2. Method of analysis and assumptions

2.1. GFEM for polycrystals

Crack paths in polycrystals are computed by means of a GFEM for polycrystals [30] which, in contrast to classical FEMs, does not need a mesh generator to mimic the polycrystalline topology. As sketched in figures 1(*a*) and (*c*), it requires a simple background mesh on which the polycrystalline topology is superimposed. Meshing of the grain boundaries and junctions is not required. Being described by means of discontinuous enrichment functions, grain boundaries can cut elements, and grain junctions can be arbitrarily located within elements. This approach makes use of a displacement decomposition, where the displacement field $\boldsymbol{u}$ of a polycrystal comprising $N_{\mathcal{G}}$ grains is described by means of the standard displacement field $\hat{\boldsymbol{u}}$, which can be considered as related to the background mesh, and the enrichment displacement field $\tilde{\boldsymbol{u}}$, representing individual grains, according to [30]

$$\boldsymbol{u} = \hat{\boldsymbol{u}} + \sum_{i=1}^{N_{\mathcal{G}}} \mathcal{H}_i \tilde{\boldsymbol{u}}_i, \tag{1}$$

where the generalized $\mathcal{H}_i$ function is equal to 1 in grain i and 0 otherwise. When considered in the construction of the weak form of the governing equations, such displacement decomposition gives rise to $N_{\mathcal{G}} + 1$ coupled weak variational statements. Each of the $N_{\mathcal{G}}$ statements corresponding to the grain structure is equipped with a traction–separation law acting across

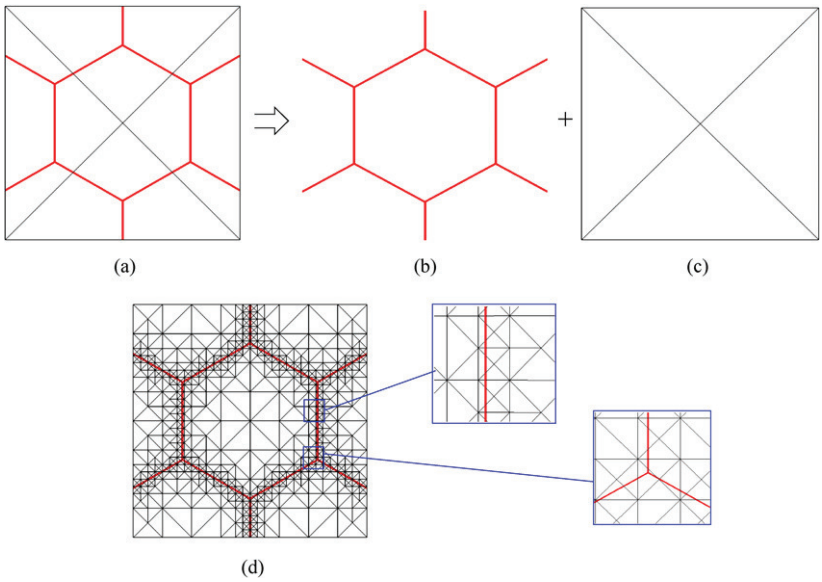

Figure 1. In the GFEM for polycrystals (*a*), a polycrystalline aggregate is described by superimposing a polycrystalline topology (*b*) on a background mesh (*c*). The quality of the numerical solution can be improved by local mesh refinement (*d*). Note that the finite element mesh does not conform to grain boundaries and junctions.

the grain boundary shared by two neighboring grains. More details can be found in [30]. The model is completed by employing a constitutive relationship describing the material behavior within the grains. The constitutive relation has been consistently linearized in a full Newton–Raphson algorithm and we observed quadratic convergence rate.

2.2. *Test setup and material*

2.2.1. Geometry and boundary conditions. The geometry and boundary conditions of the test setup are reported in figure 2. The notched specimen is loaded by a uniform tensile stress, σ, which is varied incrementally under quasi-static loading conditions. A dissipation-based arc-length procedure [14] was employed in order to trace the complex load–displacement curves, which are characterized by the frequent snap-backs associated with the failure of individual grain boundaries. The boundary conditions are such that the specimen ends can rotate freely so that the crack is not restrained by the specimen geometry.

We have considered many random realizations of an 80 grain polycrystalline topology inside the process zone depicted in figure 2. Each random realization is generated from a regular hexagonal topology by offsetting each grain junction by random perturbations. We identify each realization by means of an empirical non-dimensional randomness parameter $\bar{\rho}$ [23] which is equal to 0.289 for a regular hexagonal topology and larger for any random realization. The randomness parameter $\bar{\rho}$ is defined as the average value of the geometrical parameter

$$\rho = \frac{1}{K A_{\mathrm{G}}} \sum_{k=1}^{K} L^{(k)^2} \left[1 + \sin\left(2\psi^{(k)}\right)\right] \tag{2}$$

over all grains. The parameter ρ in turn is defined at the grain level considering the number K of grain-boundary facets, the grain area A_{G}, the length $L^{(k)}$ of the part that lies within the

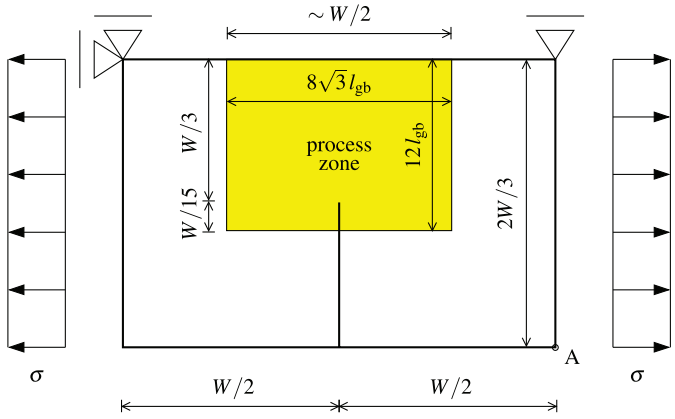

Figure 2. Geometry and boundary conditions for the notched specimen employed in the simulations. The process zone is the region in which grains and grain boundaries are represented explicitly; outside this zone the material is a homogeneous continuum.

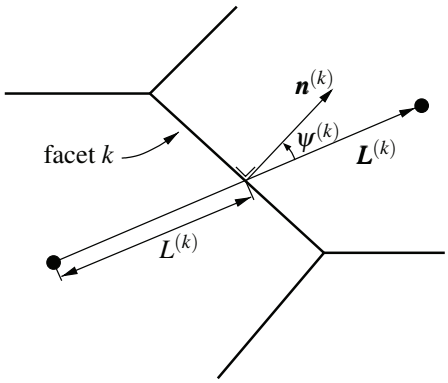

Figure 3. Definition of quantities for the computation of the randomness parameter ρ (adapted from [23]).

grain of the vector $\boldsymbol{L}^{(k)}$ connecting the centroids of the grains adjacent to facet k, and the angle between the normal $\boldsymbol{n}^{(k)}$ to facet k and $\boldsymbol{L}^{(k)}$, see figure 3.

The average grain size is defined here as the distance between two opposite sides of a hexagonal grain in the regular hexagonal topology. This quantity turns out to be very close to the average grain size computed from randomized hexagonal topologies. In the simulations, we have considered an average grain size of approximately 21 μm, similar to the values used by Zavattieri *et al* [41] (22 μm) and Kraft and Molinari [16] (25 μm), which corresponds to an average grain-boundary length $l_{\mathrm{gb}} \approx 12\,\mu$m. With around 80 grains in the process zone inside the ligament area, as indicated in figure 2, the length of the specimen is $W = 360\,\mu$m.

2.2.2. Bulk behavior. The material parameters are taken to be representative of an average polycrystalline alumina, Al_2O_3. We assume the grains to be elastic and isotropic, with Young's modulus $E = 384.6\,\mathrm{GPa}$ and Poisson's ratio $\nu = 0.237$. This assumption is based on the observation by Molinari and co-workers [16, 38] that intergranular failure is not substantially affected by the elastic anisotropy of polycrystalline alumina. The plane strain analyses are

performed under the assumption of small elastic strains and rotations. The model will not be able to capture grain rotation if the crack opening becomes large.

2.2.3. Grain-boundary behavior. Non-linearity in the material response is defined by the cohesive law across grain boundaries. In this study, we have used the Xu–Needleman cohesive law [40] and considered variations of the cohesive strength and the fracture energy with the understanding that only these two parameters and not the shape of the cohesive law matter [1, 33]. The Xu–Needleman cohesive law is a potential-based cohesive zone model involving an initial compliance representing that of the grain boundary. In this cohesive law, the tractions in normal and tangential direction, respectively, are given by

$$T_{\mathrm{n}} = \frac{\phi_{\mathrm{n}}}{\delta_{\mathrm{n}}} \exp\left(-\frac{\Delta_{\mathrm{n}}}{\delta_{\mathrm{n}}}\right) \left\{ \frac{\Delta_{\mathrm{n}}}{\delta_{\mathrm{n}}} \exp\left(-\frac{\Delta_{\mathrm{t}}^2}{\delta_{\mathrm{t}}^2}\right) + \frac{1-q}{r-1} \left[1 - \exp\left(-\frac{\Delta_{\mathrm{t}}^2}{\delta_{\mathrm{t}}^2}\right)\right] \left[r - \frac{\Delta_{\mathrm{n}}}{\delta_{\mathrm{n}}}\right] \right\} \tag{3}$$

and

$$T_{\mathrm{t}} = 2\left(\frac{\phi_{\mathrm{n}}\Delta_{\mathrm{t}}}{\delta_{\mathrm{t}}^2}\right) \left\{ q + \left(\frac{r-q}{r-1}\right) \frac{\Delta_{\mathrm{n}}}{\delta_{\mathrm{n}}} \right\} \exp\left(-\frac{\Delta_{\mathrm{n}}}{\delta_{\mathrm{n}}}\right) \exp\left(-\frac{\Delta_{\mathrm{t}}^2}{\delta_{\mathrm{t}}^2}\right) \tag{4}$$

in terms of the normal and tangential opening Δ_{n} and Δ_{t}. In the above relations, ϕ_{n} is the work of normal separation, ϕ_{t} is the work of tangential separation, while δ_{n} and δ_{t} are the openings corresponding to the uncoupled normal and tangential strengths. The normal strength itself is then given by $\sigma_{\max} = \exp(-1)\phi_{\mathrm{n}}/\delta_{\mathrm{n}}$. Coupling between normal and tangential directions is achieved by the parameters $q = \phi_{\mathrm{t}}/\phi_{\mathrm{n}}$ and $r = \Delta_{\mathrm{n}}^*/\delta_{\mathrm{n}}$, with Δ_{n}^* being the normal opening after complete shear separation at $T_{\mathrm{n}} = 0$. In line with previous works on mesoscopic failure analysis of alumina with cohesive zone elements [18, 41], we have selected $q = 1$. It is worth noting that $q = 1$ is the only value of this parameter for which the Xu–Needleman cohesive law can properly describe coupling between normal and tangential directions [34]. When $q = 1$, it can be observed from (3) and (4) that the value of r does not have any influence in the cohesive law.

In the original Xu–Needleman model [40], the cohesive zone law is assumed to be reversible. In line with other studies on mesoscopic failure of polycrystalline aggregates [7, 41], we have considered secant unloading in the numerical analyses performed in this study. We have, however, compared the response of a few cases considering both reversible behavior and secant unloading and found very small differences in some parts of the unloading/reloading branches of the load–displacement curves. These differences can be seen in the curves in figure 4 obtained for one of the polycrystalline topologies employed in section 3. Both options resulted in the same crack path.

In our numerical simulations, a 'crack' develops when the crack openings are larger than the corresponding characteristic separation values, i.e. when $\Delta_{\mathrm{n}} > \delta_{\mathrm{n}}$ or $\Delta_{\mathrm{t}} > \delta_{\mathrm{t}}$. All crack paths have therefore been drawn using this definition. Although other approaches might be more appropriate to define a crack, the reported cracks are related to the end of the loading process, when a crack is fully developed and almost all the cohesive energy has been dissipated. In fact, the simulations have been stopped when the resultant of the stress σ acting on the right side of the specimen is less than one thousandth of the applied load—this corresponds to a horizontal displacement of point A in figure 2 of maximum 5 μm; for the sake of clarity in the representation of these curves we have decided to show only the 'interesting' part, thus restricting the range of the horizontal axis. Similar to other authors [18, 41], and dictated by lack of precise knowledge, the characteristic separations in normal and tangential direction are set to be equal ($\delta_{\mathrm{n}} = \delta_{\mathrm{t}}$); this choice is discussed further in section 3.5. For any choice of the normal strength $\sigma_{\max}$ and fracture energy $\phi_{\mathrm{n}} = G_{\mathrm{Ic}}$, the value of δ_{n} is computed considering that $\phi_{\mathrm{n}} = \sigma_{\max} \exp(1)\delta_{\mathrm{n}}$ [40].

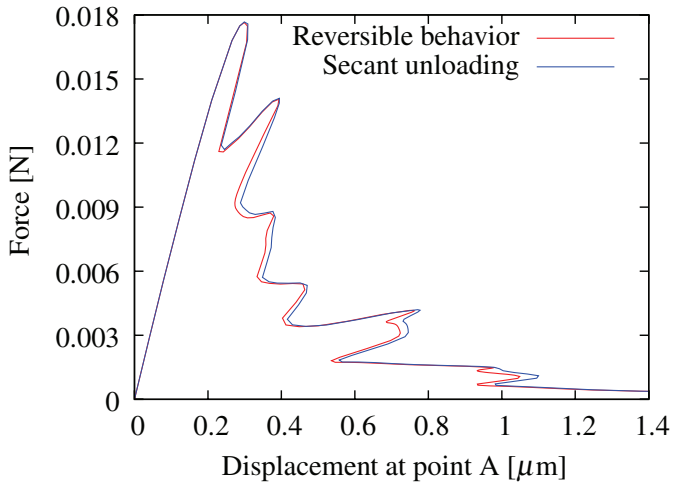

Figure 4. Influence of the unloading behavior in the cohesive law (reversible behavior versus secant unloading).

2.2.4. Grain-boundary cohesive strength and critical fracture energy. Grain boundary cohesive strength, σ_{max}, and critical fracture energy, G_{Ic}, depend both on grain-boundary size [25, 26]. According to Rice [26] (figure 3), the tensile strength σ_{max} of alumina is around 0.4 GPa for 21 μm grains. Zavattieri *et al* [41] considered σ_{max} from 1 to 10 GPa for 22 μm grains while Kraft and Molinari [16] considered $\sigma_{max} = 0.6$ GPa for 25 μm grains. In the first set of simulations to be reported in section 3, we consider values from 0.6 to 3.0 GPa. In section 4, this range is broadened to 0.384–3.84 GPa.

Regarding the critical fracture energy G_{Ic}, Rice *et al* [25] (figure 5) report values between 35 and 45 J m^{-2} for grain sizes around 21 μm. Kraft and Molinari [16] considered several distributions of the fracture energy G_{Ic} over the grain boundaries with values between 1 and 22 J m^{-2}. Based on these figures, we consider values of G_{Ic} between 7.09 and 39.3 J m^{-2} as in Zavattieri *et al* [41].

2.3. Mesh related issues

We have employed meshes of constant strain triangular elements which, when intersected by grain boundaries, are refined to the desired level as shown in figure 1. A longest-edge mesh refinement algorithm [27] is used for this purpose. An obvious advantage of this approach is that this local refinement algorithm preserves the aspect ratio of the elements in the mesh throughout the refinement process with the added benefit of not having to constrain the mesh to the local features of the problem (grain boundaries and junctions in our case) [10].

The mesh along grain boundaries must be sufficiently fine in order to resolve the length scale associated with the cohesive law. To resolve the cohesive law along grain boundaries, considered as discontinuities in GFEM, each discontinuity segment length l_d, defined by the intersection between an element and a grain boundary as shown in figure 5, needs to be, at least, smaller than the cohesive length l_z. This bound on discontinuity segments is met by making the length l_e of the longest side of all the elements intersected by grain boundaries $\leqslant l_z$. For potential-based cohesive laws this parameter is estimated as [12]

$$l_z = \frac{9\pi}{32}\frac{E}{1-\nu^2}\frac{G_{Ic}}{\sigma_{max}^2}. \tag{5}$$

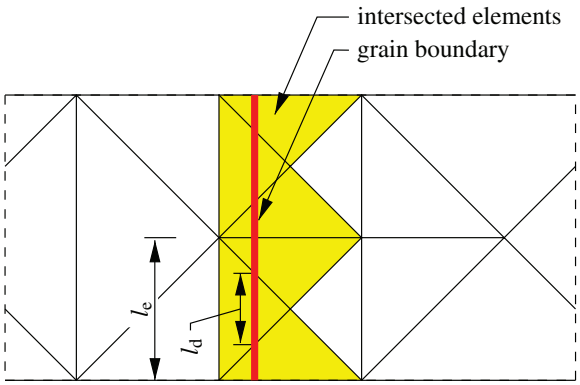

Figure 5. Definition of discontinuity segment length, l_d, and length of the longest element side associated with elements crossed by a discontinuity, l_e.

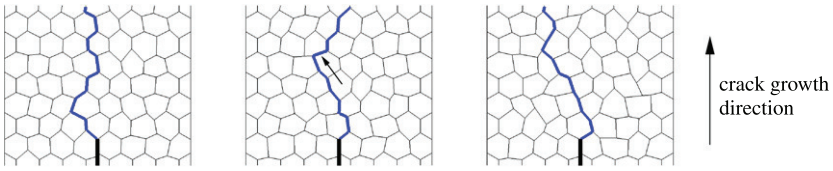

(a) realization 1 (b) realization 2 (c) realization 3

Figure 6. Three different realizations of 80 grains in the process zone. The blue line indicates the computed crack path for $G_{Ic} = 39.3\,J\,m^{-2}$ and $\sigma_{max} = 0.6\,GPa$, while the thick black line indicates the traction-free notch. The arrow in (*b*) points to the grain boundary for which the traction profile is presented in figure 12.

In the traditional FEM with conforming meshes, reliable results can be obtained by specifying a minimum number of elements in the cohesive zone. There is, however, no consensus on the value of this number: Carpinteri and Colombo [5], according to [20], suggested to use more than ten elements; Falk *et al* [12] used two to five elements in their analyses; Moës and Belytschko [20] suggested a minimum of two elements; Turon *et al* [32] and Harper and Hallett [15] proposed at least three elements in a fully developed cohesive zone, while Sfantos and Aliabadi [29] used at least 15 elements. These figures make reference to problems as diverse as delamination and crack propagation in homogeneous materials thus suggesting the existence of a problem-dependent estimate of the minimum number of elements required in the cohesive zone. Therefore, we devote a separate section in the following to estimate the necessary number of elements for our problem of brittle cracking in polycrystals.

3. Results and discussion

We have performed mesh refinement and parametric studies to evaluate the impact of cohesive law parameters on the crack path. These studies were carried out considering the three different random realizations of an 80 grain hexagonal polycrystalline topology shown in figure 6.

It is worth noting that in this study we are drawing conclusions about crack paths and not about the position of the crack tip—crack paths are not sensitive to the precise criterion used to define the crack tip.

3.1. Mesh refinement studies

Figure 5 depicts a typical situation arising from the intersection between an element and a grain boundary. We have performed a mesh refinement study to establish the length l_e that can be used with confidence in the rest of our investigations. This length must be such that any other discretization with smaller lengths l_e yields the same crack path and load–displacement curve. Two sets of analyses are considered for this purpose. In both, $G_{Ic} = 39.3\,\mathrm{J\,m^{-2}}$ but the cohesive strength is varied so as to cover a range of cohesive lengths l_z through (5).

In the first set of analyses, the cohesive strength σ_{max} is taken as 3.0 GPa which corresponds to a cohesive length $l_z = 1.57\,\mu$m. Two refinement levels are considered. One with element sides $l_e \approx l_z$ and the other with $l_e \approx l_z/3$. Since discontinuities can cross elements, these constraints on l_z must be considered as upper bounds on element side lengths as is evident from figure 1(*d*). Further, to avoid the use of unreasonably coarse meshes, we require at least four intersecting elements along each grain boundary as well as $l_e \leqslant l_{gb}/2$. These constraints have been imposed on all the meshes used in this study.

The results of the mesh refinement study are shown in figure 6. We found that crack paths obtained with both refinement levels are identical. This seems to suggest that considering element sides l_e approximately equal to l_z is adequate. To confirm this, we consider a second set of analyses, with two refinement levels, in which the cohesive strength σ_{max} takes values 0.6, 1.0 and 2.0 GPa, corresponding to cohesive lengths equal to 39.3, 14.1 and 3.53 μm; the values of δ_n and δ_t were adapted to σ_{max} in order to dissipate the same fracture energy. Unlike the previous set of analyses, we found that in two out of nine cases (realizations 1 and 2 with $\sigma_{max} = 2.0$ GPa), the two refinement levels yielded different crack paths as reported in figure 7. Further, the crack paths obtained with element sides approximately equal to $l_z/3$ resulted identical to those reported in figure 6. In all the other cases, crack paths obtained with the two refinement levels were identical. This raises the question of whether the crack paths obtained with element sides $l_e \approx l_z/3$ can be accepted with confidence. A further mesh refinement study, not reported here, was done reconsidering some of the 12 cases described so far to check if the use of smaller elements in regions crossed by discontinuities would result in different crack paths. We found no differences in the crack paths.

Thus, this study suggests a mesh refinement such that the length of the longest side of all the elements intersected by grain boundaries $l_e \leqslant \min(l_z/3, l_{gb}/2)$ with at least four intersecting elements along each grain boundary. We assume that the same bounds apply for any value of l_z.

3.2. Effect of cohesive strength on fracture behavior

In the above mesh refinement study, we have already considered variations of the cohesive strength σ_{max}. The crack paths obtained with this set of parameters are identical and were reported in figure 6. Nevertheless, since the grain boundaries have varying strength, the load–displacement curves are different, as shown in figure 8. It is noted that, when considering the bounds on element size defined in section 3.1, increasing the cohesive strength gives rise to a distinct raggedness of the curves as seen in figures 8(*c*) and (*d*). This is due to the limited resolution of the cohesive law along cracking grain boundaries. The load–displacement curves can indeed be smoothed using finer meshes as shown in figure 9 for the case reported in figure 8(*c*). This procedure, however, is very costly because of the large number of degrees of freedom involved, and it does not result in any change of the crack path solution while the improvement in the load–displacement curve is arguably of 'cosmetic' nature.

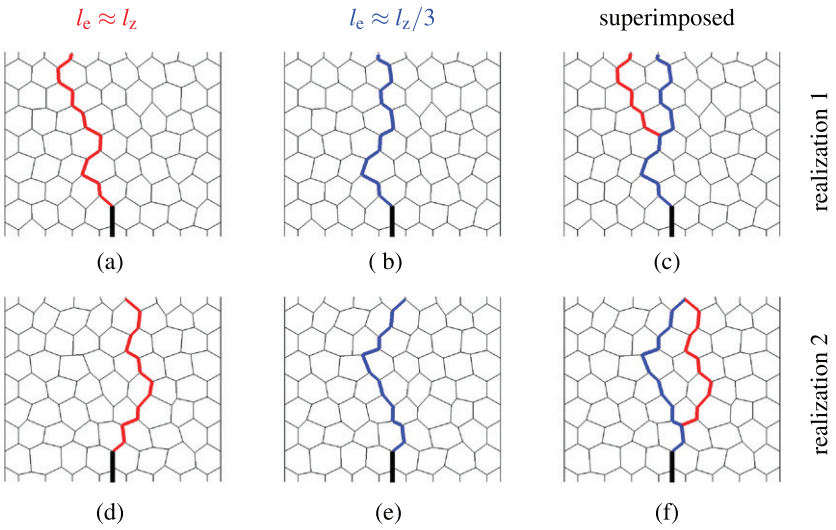

Figure 7. Sensitivity of the crack path to mesh refinement for $\sigma_{max} = 2.0\,GPa$ and $G_{Ic} = 39.3\,J\,m^{-2}$ for realizations 1 and 2: crack path obtained with element sides $l_e \approx l_z$ (a), (d) and $l_e \approx l_z/3$ (b), (e); superimposed cracks paths (c), (f).

Based on these observations, we conclude that the crack path is not affected by the magnitude of σ_{max} in the selected range, and that the load–displacement curves are qualitatively similar. Consequently, crack paths and load–displacement curves obtained for low cohesive strength, being cheaper and easier to compute, can be considered valid also for higher strengths.

3.3. Effect of critical fracture energy on fracture behavior

To study the effect of the critical fracture energy on the crack path, G_{Ic} is set equal to 7.09, 11.4, 22.1 and $39.3\,J\,m^{-2}$, while keeping $\sigma_{max} = 0.6\,GPa$. Similar to the cases described in the previous section, no difference in the crack paths is found with respect to those reported in figure 6. The load–displacement curves, depicted in figure 10 for realization 2, show a serrated behavior similar to that reported in figure 8. However, unlike the latter, the load–displacement curves in figure 10 do reveal quantitative differences in terms of the dissipated energy as a consequence of the change in fracture energy. Directly related to the fracture energy is the number of degrees of freedom used in the simulations. This quantity decreases with increasing fracture energy G_{Ic} since l_e scales with G_{Ic} via l_z according to (5). Further, increasing values of the fracture energy correspond to smoother curves as shown in figure 10. This is again related to the resolution of the cohesive law along grain boundaries.

To further confirm these observations on the crack path and the features of the load–displacement curve, realization 2 is reconsidered with $\sigma_{max} = 2\,GPa$ using the same set of values for G_{Ic}. Apart from being computationally more demanding, the load–displacement curves, not reported here, show features similar to those just described for $\sigma_{max} = 0.6\,GPa$, and the crack paths are also identical to the one reported in figure 6(b).

The observations gathered so far suggest that, for a given arrangement of grains and in the range considered for the parameters, the crack path is independent of the cohesive strength and fracture energy.

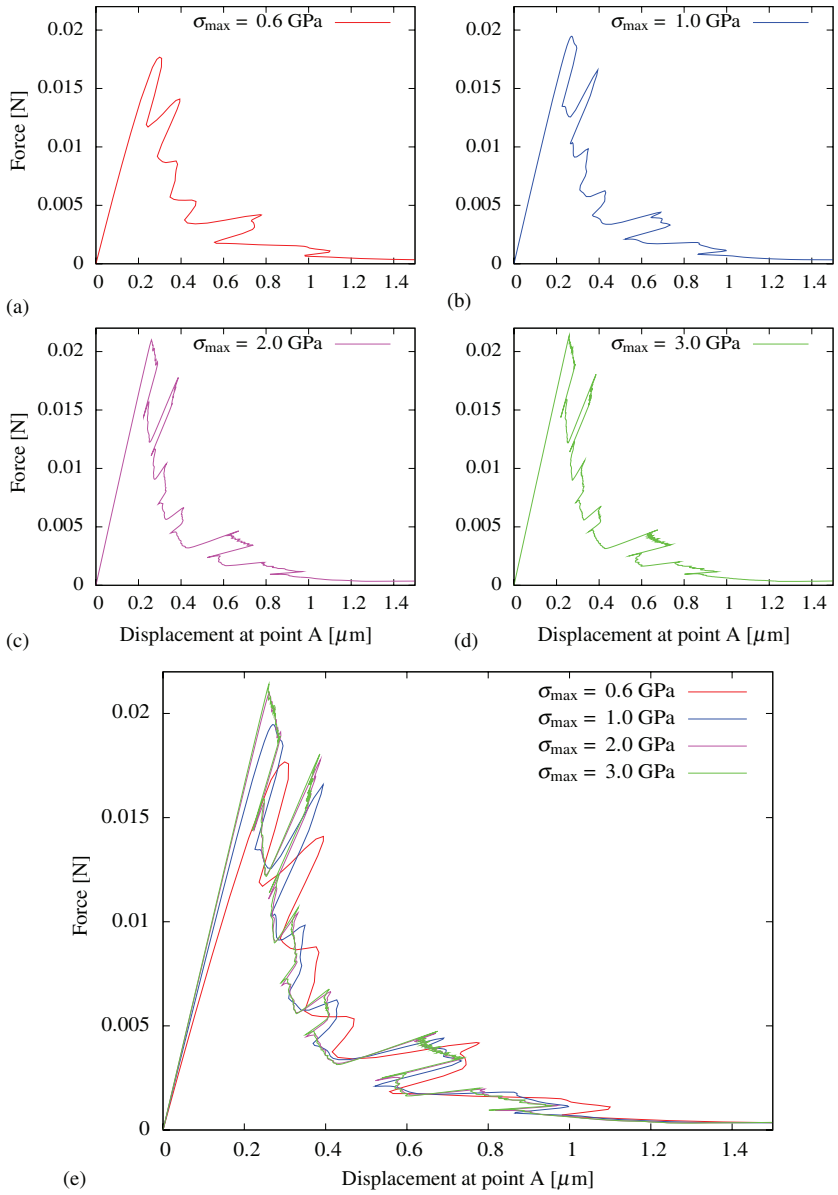

Figure 8. Load–displacement curves for an 80 grain topology (realization 2) with $G_{\mathrm{Ic}} = 39.3\,\mathrm{J\,m^{-2}}$ using different values of $\sigma_{\max}$: (*a*) $\sigma_{\max} = 0.6\,\mathrm{GPa}$, (*b*) $\sigma_{\max} = 1\,\mathrm{GPa}$, (*c*) $\sigma_{\max} = 2\,\mathrm{GPa}$, (*d*) $\sigma_{\max} = 3\,\mathrm{GPa}$, (*e*) superposition. The net force reported on the vertical axis is the resultant of the stress σ acting on the right side of the specimen.

3.4. Intragranular stress and intergranular traction fields

After having considered overall fracture characteristics, it is interesting at this point to study the stress fields inside grains and the normal traction profiles along grain boundaries. These characteristics in a region around the propagating crack tip are shown in figure 12 for different values of fracture energy and cohesive strength.

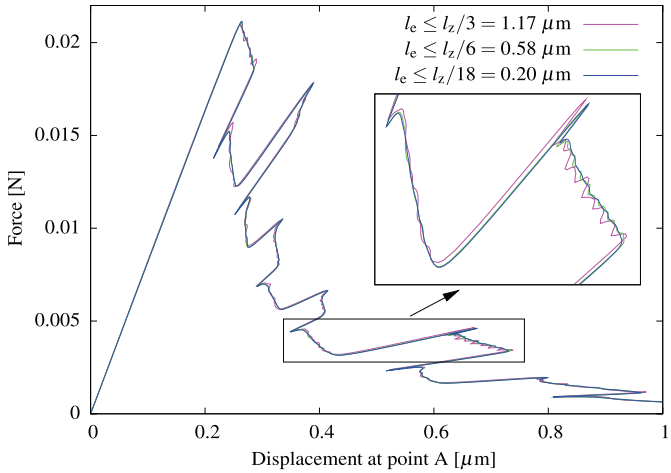

Figure 9. Effect of mesh refinement on the load–displacement curve for realization 2 with $\sigma_{max} = 2$ GPa and $G_{Ic} = 39.3\,\mathrm{J\,m^{-2}}$ (refer to figure 8(*c*)).

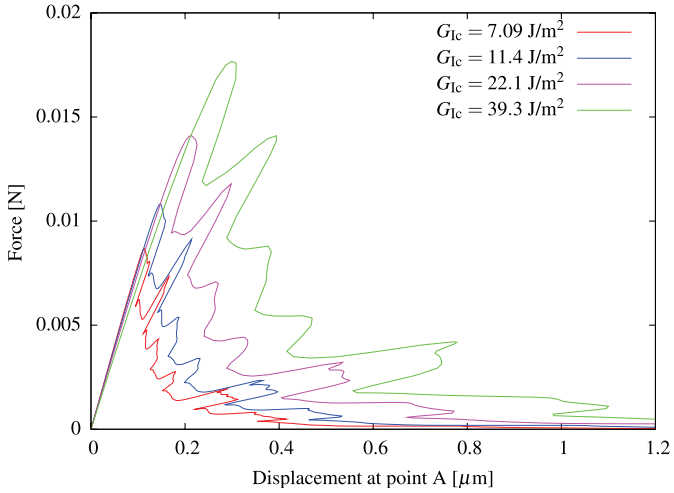

Figure 10. Load–displacement curves for an 80 grain topology (realization 2) using different values of fracture energy G_{Ic} with cohesive strength $\sigma_{max} = 0.6$ GPa.

In contrast to the observation above that the crack paths are identical to the one reported in figure 6(*b*), figure 12 reveals a rich palette in stress fields inside grains and traction distribution along grain boundaries. It is quite remarkable that not even the extent of the inelastic region ahead of the crack tip—determined by the cohesive length l_z—has a significant influence on the crack path. In fact, identical crack paths are obtained in the two extreme cases reported in figures 12(*c*)–(*f*) where $l_z = 0.638\ \mu$m and 39.3 μm, respectively.

It is worth noting that in the case of figure 12(*c*) and (*d*) the cohesive length $l_z = 0.638\ \mu$m is smaller than 1.57 μm which was the smallest value considered in the definition of the bounds on element size in section 3.1. However, the evidence that the same crack path is obtained with all four values of the cohesive length confirms, indirectly, the validity of the proposed bounds on element size.

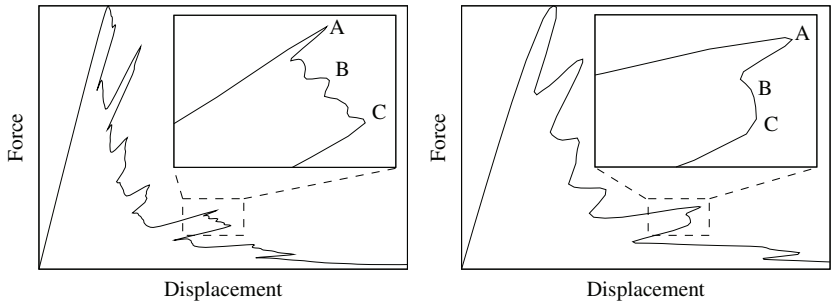

Figure 11. Sampling points for the stress fields and traction profiles reported in figure 12.

In conclusion, in the cases considered so far, the relative arrangement of grains in a polycrystal seems to be the only important factor in the definition of the crack path.

3.5. Energy balance: relative contribution of normal and tangential energies

We have computed the dissipated energy following two approaches. In the first approach, the dissipated energy at the global level, G_{glob}, is a function of the work done by the external loads and is calculated as

$$G_{\text{glob}} = \sum_{i=1}^{n} w_i, \tag{6}$$

with the global energy dissipation increments computed from

$$w_i = \tfrac{1}{2}\left[\lambda_{i-1}\left(\boldsymbol{u}_i^{\text{T}} - \boldsymbol{u}_{i-1}^{\text{T}}\right) - (\lambda_i - \lambda_{i-1})\,\boldsymbol{u}_{i-1}^{\text{T}}\right]\hat{\boldsymbol{f}}. \tag{7}$$

Here, i is an index running on the n load increments, λ_i is the incremental loading factor, $\boldsymbol{u}_i$ is the displacement solution vector, and the unit force vector $\hat{\boldsymbol{f}}$ is related to the external force vector $\boldsymbol{f}^{\text{ext}}$ through $\boldsymbol{f}^{\text{ext}} = \lambda\hat{\boldsymbol{f}}$ where λ is a load factor. More details on the derivation of the energy increments can be found in [14]. In the second approach, the dissipated energy at the local level, G_{loc}, is computed along the grain boundaries considering the same expression (i.e. (6) and (7)) now made a function of displacement jumps and tractions across each discontinuity segment according to

$$G_{\text{loc}} = G_{\text{n,loc}} + G_{\text{t,loc}}, \tag{8}$$

with the normal and tangential contributions

$$G_{\text{n,loc}} = \sum_{i=1}^{n} w_{\text{n}_i} \qquad \text{and} \qquad G_{\text{t,loc}} = \sum_{i=1}^{n} w_{\text{t}_i}, \tag{9}$$

and incremental energies defined as

$$w_{\text{n}_i} = \sum_{j=1}^{n_{\text{l}_\text{d}}} \frac{1}{2} \int_{\Gamma_{\text{d}_j}} \left[T_{\text{n}_{i-1}}\left(\Delta_{\text{n}_i} - \Delta_{\text{n}_{i-1}}\right) - \left(T_{\text{n}_i} - T_{\text{n}_{i-1}}\right)\Delta_{\text{n}_{i-1}}\right] \text{d}\Gamma_{\text{d}_j} \tag{10}$$

and

$$w_{\text{t}_i} = \sum_{j=1}^{n_{\text{l}_\text{d}}} \frac{1}{2} \int_{\Gamma_{\text{d}_j}} \left[T_{\text{t}_{i-1}}\left(\Delta_{\text{t}_i} - \Delta_{\text{t}_{i-1}}\right) - \left(T_{\text{t}_i} - T_{\text{t}_{i-1}}\right)\Delta_{\text{t}_{i-1}}\right] \text{d}\Gamma_{\text{d}_j}, \tag{11}$$

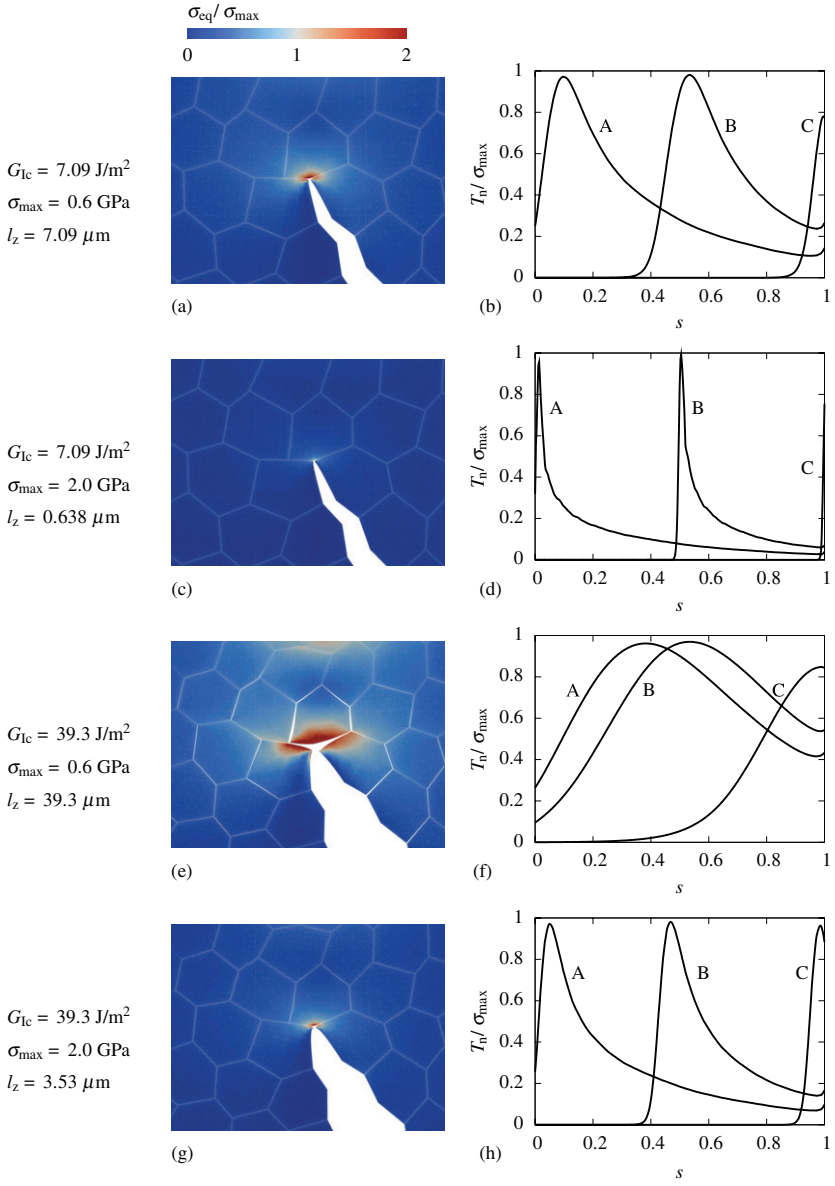

Figure 12. Failure characterization for the polycrystal in figure 6(*b*) (realization 2). Left column: local failure pattern (50× displacement magnification) and normalized von Mises equivalent stress sampled at point A in figure 11. Right column: evolution of the normal traction profile along the grain boundary indicated by an arrow in figure 6(*b*) (*s* is the normalized coordinate along the grain boundary and its origin coincides with the crack tip; the crack tip is located at the left-hand side of the arrow in figure 6(*b*); sampling points A, B and C are indicated in figure 11; element size $l_e \approx 0.20\,\mu$m).

where n_{l_d} is the total number of discontinuity segments, Γ_{d_j} denotes the length of jth discontinuity segment, T_n and T_t are the tractions and Δ_n and Δ_t are the local jumps in the normal and tangential directions, respectively. Both energies are then compared by considering various mesh refinement levels and two sets of grain-boundary properties: $G_{Ic} = 39.3\,\mathrm{J\,m^{-2}}$

Table 1. Comparison of global energy G_{glob}, related to the work done by the external loads, and local energy G_{loc}, dissipated along grain boundaries ($G_{Ic} = 39.3\,J\,m^{-2}$, $\sigma_{max} = 0.6\,GPa$, $l_z = 39.3\,\mu m$).

	l_e (μm)	$\frac{l_e}{l_z}$ (—)	G_{glob} (nJ)	$G_{loc} = G_{n,loc} + G_{t,loc}$ (nJ)	$\frac{G_{n,loc}}{G_{loc}}$ (%)	$\frac{G_{t,loc}}{G_{loc}}$ (%)	$\frac{G_{loc} - G_{glob}}{G_{glob}}$ (%)
Realization 1	6.05	$\leqslant$1/6	6.48	8.94	86.0	14.0	38.1
($\bar{\rho} = 0.355$)	4.25	$\leqslant$1/9	6.54	7.92	85.8	14.2	21.2
	2.00	$\leqslant$1/19	6.44	7.18	85.4	14.6	11.5
	0.50	$\leqslant$1/78	6.44	6.61	85.6	14.4	2.74
	0.20	$\leqslant$1/196	6.42	6.51	85.7	14.3	1.31
Realization 2	6.05	$\leqslant$1/6	6.21	8.72	86.8	13.2	40.3
($\bar{\rho} = 0.376$)	4.25	$\leqslant$1/9	6.20	7.47	86.8	13.2	20.6
	2.00	$\leqslant$1/19	6.19	6.89	86.9	13.1	11.3
	0.50	$\leqslant$1/78	6.17	6.35	87.4	12.6	2.90
	0.20	$\leqslant$1/196	6.17	6.26	87.7	12.3	1.33
Realization 3	6.05	$\leqslant$1/6	5.90	8.50	88.7	11.3	44.0
($\bar{\rho} = 0.400$)	4.25	$\leqslant$1/9	5.90	7.27	88.2	11.8	23.2
	2.00	$\leqslant$1/19	5.90	6.61	87.9	12.1	12.0
	0.50	$\leqslant$1/78	5.89	6.05	88.1	11.9	2.75
	0.20	$\leqslant$1/196	5.89	5.97	88.3	11.7	1.39

with $\sigma_{max} = 0.6$ (table 1) and 2.0 GPa (table 2). The refinement level is shown in the second column in terms of the length l_e of the longest side of all the elements intersected by grain boundaries.

From the results shown in tables 1 and 2, it can be observed that (i) the relative error between local and global energies (last column) depends only on the mesh refinement level in terms of l_e—further analyses performed with the three realizations shown in figure 6 and considering variations of cohesive strength and fracture energy confirm this observation and the results are reported in figure 13; (ii) the calculated global energy is almost insensitive to the mesh density (fourth column); (iii) the contribution from normal energy dissipation $G_{n,loc}$ to the local energy is around 90% showing a mode-I dominated cracking behavior (sixth column); (iv) normal and tangential contributions do not vary significantly with refinement (sixth and seventh columns).

A few representative cases have been re-examined by varying the value of δ_t/δ_n over a decade compared with the reference value of 1. When δ_t/δ_n is less than 0.9, our simulations experienced convergence problems, which could be traced back to the fact that small values of δ_t/δ_n obstruct grain-boundary sliding, which is a necessary condition to develop a crack in polycrystals under mode-I loading at the specimen level. Values of δ_t/δ_n equal to/greater than 0.9 resulted in the same crack path and more or less the same energy contributions as reported in tables 1 and 2. Large values of δ_t/δ_n, however, resulted in different crack paths in some cases due to particular grain arrangements (refer to the discussion in section 4 and figure 16). In addition, in all completed analyses, the percentage difference in global and local energies has been found to be very close to that reported for $\delta_t/\delta_n = 1$ for all the examined values of the ratio δ_t/δ_n.

3.6. Topologies generated by centroidal Voronoi tessellation

To demonstrate that our results are not tied to a hexagonal grain structure, we report results obtained by employing two 80 grain polycrystalline non-hexagonal topologies generated using

Table 2. Comparison of global energy G_{glob}, related to the work done by the external loads, and local energy G_{loc}, dissipated along grain boundaries ($G_{\text{Ic}} = 39.3\,\text{J m}^{-2}$, $\sigma_{\max} = 2.0\,\text{GPa}$, $l_z = 3.53\,\mu\text{m}$).

	l_e (μm)	$\frac{l_e}{l_z}$ (—)	G_{glob} (nJ)	$G_{\text{loc}} = G_{\text{n,loc}} + G_{\text{t,loc}}$ (nJ)	$\frac{G_{\text{n,loc}}}{G_{\text{loc}}}$ (%)	$\frac{G_{\text{t,loc}}}{G_{\text{loc}}}$ (%)	$\frac{G_{\text{loc}} - G_{\text{glob}}}{G_{\text{glob}}}$ (%)
Realization 1	1.17	$\leqslant$1/3	6.19	6.72	88.7	11.3	8.60
($\bar{\rho} = 0.355$)	0.58	$\leqslant$1/6	6.18	6.43	88.7	11.3	4.07
	0.20	$\leqslant$1/18	6.17	6.26	88.6	11.4	1.32
Realization 2	1.17	$\leqslant$1/3	6.04	6.53	89.8	10.2	8.23
($\bar{\rho} = 0.376$)	0.58	$\leqslant$1/6	6.03	6.28	90.0	10.0	4.16
	0.20	$\leqslant$1/18	6.02	6.10	90.3	9.70	1.32
Realization 3	1.17	$\leqslant$1/3	5.83	6.32	90.6	9.40	8.47
($\bar{\rho} = 0.400$)	0.58	$\leqslant$1/6	5.82	6.08	90.6	9.40	4.42
	0.20	$\leqslant$1/18	5.82	5.90	90.6	9.40	1.34

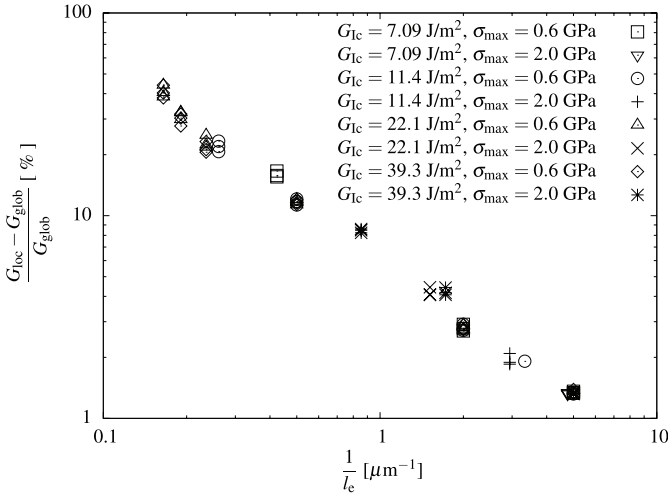

Figure 13. Convergence of local and global energy with mesh refinement.

a centroidal Voronoi tessellation algorithm. The topologies are depicted in figures 14(*a*) and 15(*a*). The blue line indicates the computed crack path obtained with different values of G_{Ic} (7.09, 11.4, 22.1 and 39.3 J m^{-2}) and $\sigma_{\max}$ (0.6 and 2.0 GPa). The corresponding load–displacement curves for $\sigma_{\max} = 0.6\,\text{GPa}$ are shown in figures 14(*b*) and 15(*b*).

The energy contributions are listed in tables 3 and 4 and show a trend similar to that related to hexagonal microstructures (refer to tables 1 and 2). However, due to the particular grain-boundary arrangement along the crack path, the topology in figure 14 dissipates more energy in the normal direction.

4. Further assessment of results

In order to confirm the representativeness of the hexagonal grain results obtained so far, 122 more realizations with $\bar{\rho}$ ranging from 0.30 to 0.40 are considered. We also enlarge the range of the grain-boundary cohesive strength $\sigma_{\max}$ considering the following three options for each

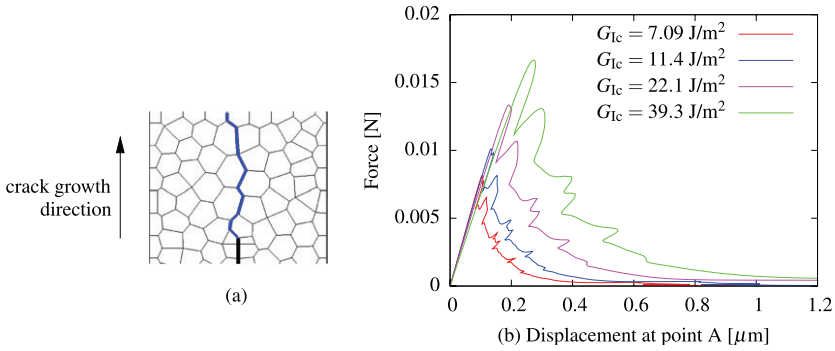

Figure 14. Crack path (*a*) and load–displacement curves (*b*) for an 80 grain polycrystalline non-hexagonal topology generated using a centroidal Voronoi tessellation algorithm. The load–displacement curves have been obtained with cohesive strength $\sigma_{max} = 0.6$ GPa.

Table 3. Comparison of global energy G_{glob}, related to the work done by the external loads, and local energy G_{loc}, dissipated along grain boundaries ($G_{Ic} = 39.3\,J\,m^{-2}$).

Figure 14(*a*)	l_e (μm)	$\frac{l_e}{l_z}$ (—)	G_{glob} (nJ)	$G_{loc} = G_{n,loc} + G_{t,loc}$ (nJ)	$\frac{G_{n,loc}}{G_{loc}}$ (%)	$\frac{G_{t,loc}}{G_{loc}}$ (%)	$\frac{G_{loc} - G_{glob}}{G_{glob}}$ (%)
$\sigma_{max} = 0.6$ GPa	4.25	$\leqslant 1/9$	5.34	6.54	88.2	11.8	22.54
($l_z = 39.3\,\mu$m)	0.20	$\leqslant 1/196$	5.33	5.41	89.5	10.5	1.52
$\sigma_{max} = 2.0$ GPa	1.17	$\leqslant 1/3$	5.33	5.76	93.1	6.9	8.20
($l_z = 3.53\,\mu$m)	0.20	$\leqslant 1/18$	5.32	5.40	93.5	6.5	1.49

Table 4. Comparison of global energy G_{glob}, related to the work done by the external loads, and local energy G_{loc}, dissipated along grain boundaries ($G_{Ic} = 39.3\,J\,m^{-2}$).

Figure 15(*a*)	l_e (μm)	$\frac{l_e}{l_z}$ (—)	G_{glob} (nJ)	$G_{loc} = G_{n,loc} + G_{t,loc}$ (nJ)	$\frac{G_{n,loc}}{G_{loc}}$ (%)	$\frac{G_{t,loc}}{G_{loc}}$ (%)	$\frac{G_{loc} - G_{glob}}{G_{glob}}$ (%)
$\sigma_{max} = 0.6$ GPa	4.25	$\leqslant 1/9$	5.86	6.83	86.0	14.1	16.46
($l_z = 39.3\,\mu$m)	0.20	$\leqslant 1/196$	5.86	5.94	87.3	12.7	1.33
$\sigma_{max} = 2.0$ GPa	1.17	$\leqslant 1/3$	5.78	6.21	90.1	9.9	7.45
($l_z = 3.53\,\mu$m)	0.20	$\leqslant 1/18$	5.77	5.84	90.6	9.4	1.33

realization: (1) $\sigma_{max} = 0.384$ GPa and $G_{Ic} = 39.3\,J\,m^{-2}$ ($l_z = 95.9\,\mu$m), (2) $\sigma_{max} = 0.384$ GPa and $G_{Ic} = 7.09\,J\,m^{-2}$ ($l_z = 17.3\,\mu$m) and (3) $\sigma_{max} = 3.84$ GPa and $G_{Ic} = 39.3\,J\,m^{-2}$ ($l_z = 0.959\,\mu$m). Seventy-one realizations resulted in identical crack paths for all options. The remaining cases have partial overlaps of the crack path and are characterized by patches of grain arrangements with peculiar geometrical features. These are cases for which it is difficult to obtain reliable results unless a very high mesh density is considered. A typical case is shown in figure 16(*a*) with crack paths corresponding to the use of two different sets of material properties reported in figures 16(*b*) and (*c*). The superposition of the two crack paths in figure 16(*d*) clearly shows that the crack path changes its direction at a junction where two grain boundaries in front of the crack tip are arranged in a Y-like configuration consisting of these two grain boundaries and the previous crack segment.

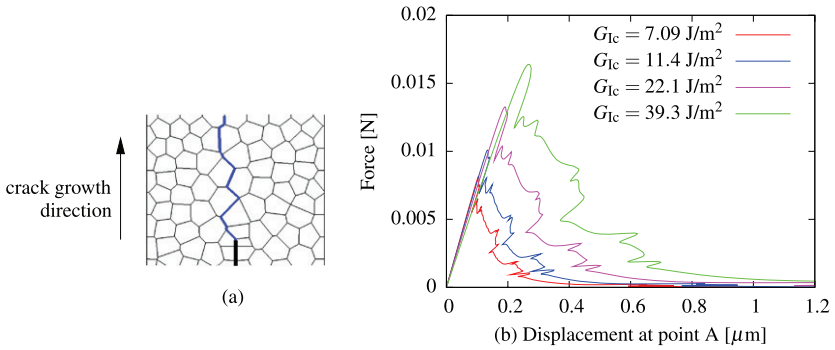

Figure 15. Crack path (*a*) and load–displacement curves (*b*) for an 80 grain polycrystalline non-hexagonal topology generated using a centroidal Voronoi tessellation algorithm. The load–displacement curves have been obtained with cohesive strength $\sigma_{max} = 0.6$ GPa.

To appreciate the influence of the grain arrangement, the position of one of the grain junctions is changed as shown in figure 16(*e*) resulting in the polycrystal in figure 16(*f*). Identical crack paths, shown in figure 16(*g*), are now obtained with this new configuration considering the same material parameters used for the simulations related to figure 16(*d*) and the same spatial discretization. Note that the loading direction is horizontal and the crack segment below the crack tip is vertical thus generating a regular Y-configuration—two such cases are shown in figure 7 and have been resolved by employing a finer mesh. We have, however, experienced cases with similar behavior in which the crack segment below the crack tip was not vertical. The identification of these special cases must be done considering local geometrical features and their orientation with respect to the loading direction. It must be stressed, however, that these situations are not uncommon and the bounds on element side lengths defined in section 3.1 do not always guarantee the determination of correct crack path and load–displacement curve. Adaptive discretization schemes [4, 11, 22, 42] should be considered in these circumstances.

The relative contribution of the energy dissipated in the normal direction along grain boundaries for the above 71 realizations is shown in figure 17. Three observations can be made. First, when the cohesive length is larger than the average grain-boundary length, the contribution of the energy dissipated in the normal direction is strongly influenced by the granular arrangement. This influence weakens with decreasing cohesive length, as indicated by the extent of the dispersion around the best fit lines. This behavior can be rationalized by noting that the cohesive length measures the distance over which the cohesive zone is active. A larger cohesive length indicates a situation in which more energy can be dissipated along a grain boundary as shown in figure 12 (compare the cohesive zone length with the size of the process zone around the crack tip). Further, the amount of the dissipation in the normal direction is related to the inclination of the grain boundary with respect to the loading direction, i.e. dissipation in the normal direction is maximum for a grain boundary perpendicular to the loading direction and null for a grain boundary parallel to it. Hence, grain boundaries with random orientations will generate a normal energy dissipation which will be a function of the size of the cohesive zone length and of the inclination of the grain boundary with respect to the loading direction. Second, decreasing values of the cohesive length correspond to increasing values of the average contribution in the normal direction. Third, although the boundary conditions promote and achieve mode-I cracking at the specimen level, local failure at the grain-boundary level is dictated by the granular arrangement

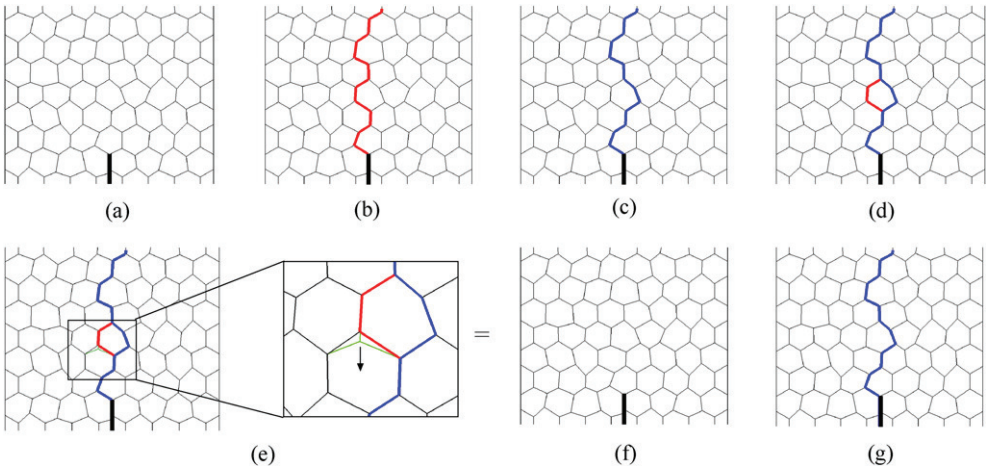

Figure 16. Influence of grain arrangement on the crack path: (*a*) original grain arrangement; (*b*), (*c*) crack paths obtained with different material properties; (*d*) superimposed crack paths; (*e*) the realization is perturbed for one of the grain boundaries in the Y-configuration as shown in the close-up; (*f*) the modified grain arrangement; (*g*) identical crack paths are obtained with different material properties.

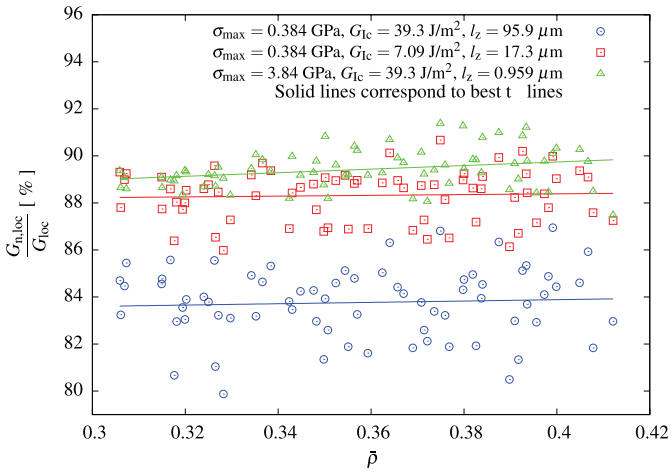

Figure 17. Relative contribution of the energy dissipated in the normal direction along grain boundaries for the 71 microstructures resulting in identical crack paths for three sets of grain-boundary properties (circle: min = 79.88%, max = 86.95%, average = 83.76%; square: min = 85.98%, max = 90.67%, average = 88.32%; triangle: min = 87.47%, max = 91.38%, average = 89.42%).

and is characterized by relative contributions in the tangential direction between 9% and 20%.

5. Summary and conclusions

Intergranular crack propagation in brittle polycrystals has been studied under quasi-static loading conditions. Various random realizations of a regular hexagonal grain topology have

been considered in combination with variations of representative values of cohesive law parameters.

Our numerical investigations suggest that mesh independent results in the GFEM for polycrystals can be obtained when the length l_e of the longest side of all the elements intersected by grain boundaries is such that $l_e \leqslant \min(l_z/3, l_{gb}/2)$ with at least four intersecting elements along each grain boundary. Following these refinement rules, we have discovered that the intergranular crack path is independent of key cohesive law parameters such as fracture energy and cohesive strength, and depends solely on the underlying microstructure. This has been confirmed on two microstructures generated with a centroidal Voronoi tessellation.

It is to be noted that the GFEM used in this paper does not provide any benefit in terms of discretization error or convergence rates. In general, enriched FEMs based on the partition of unity property of shape functions, such as the GFEM [3, 9] and XFEM [21, 31, 37], and equipped with a discontinuous enrichment function to describe interfaces and cracks, can facilitate the meshing stage of an FEM analysis. This is important when a large number of microstructures need to be discretized. Improvements in terms of discretization error or convergence rate can only be obtained with special enrichments functions or making recourse to 'classical' approaches like h- or p-refinement [10]. Since our GFEM implementation does not incorporate such extra enrichment functions, its performance can be considered comparable to that of the standard FEM equipped with cohesive zones through interface elements along grain boundaries. Indeed, as shown in [30, section 4], the solutions of both methods (GFEM and standard FEM) are the same when the grain boundaries are located along element boundaries.

Other important findings of our study can be summarized as follows.

(1) Simulations with low values of the cohesive length, related to high σ_{max} and low G_{Ic}, require very fine mesh in order to resolve the cohesive response of grain boundaries and to obtain smooth load–displacement curves. Furthermore, their complex equilibrium path can be traced only using very small load increments. Conversely, smaller σ_{max} and/or larger G_{Ic} leads to smoother load–displacement curves which can be obtained with coarser meshes. Since the crack path is insensitive to the cohesive properties, this implies that the most convenient set of cohesive parameters may be used to determine the crack path.

(2) The difference between global and local energies decreases with increasing mesh refinement, but the partitioning in normal and tangential contributions does not vary significantly. The difference between local and global energies is independent of the cohesive law parameters. Unlike the local energy, the global energy is almost insensitive to the mesh density.

(3) When the cohesive length l_z is larger than the average grain-boundary length l_{gb}, the contribution of the energy dissipated in the normal direction to the global energy is strongly influenced by the granular arrangement and the dispersion around the mean value is more pronounced. Furthermore, a decrease in the cohesive length l_z gives rise to an increase in the normal contribution to the total energy dissipation.

(4) The boundary conditions employed in the simulations promote and achieve mode-I cracking at the specimen level. However, local failure at the grain-boundary level is dictated by the granular arrangement and is characterized by relative contributions of tangential separation between 9% and 20%. Accordingly, the contribution in normal direction is between 80% and 91% showing a mode-I dominated cracking behavior—similar figures have been obtained with microstructures generated with a centroidal Voronoi tessellation as shown in section 3.6. Higher values of the normal energy contribution correspond to situations with localized sharp normal traction profiles along grain boundaries. Our results suggest that mode-I cracking in polycrystals is only possible

if the grain-boundary deformation is accommodated by sliding and normal separation. The suppression of the tangential contribution results in a kinematic constraint that is released at the expense of many grain boundaries failing in normal direction thus resulting in diffuse cracking—such simulations are usually not numerically stable and have not been reported in this study.

Acknowledgments

This research is supported by the Higher Education Commission, Pakistan. We are grateful to Frank Everdij (Faculty of Civil Engineering and Geosciences, Delft University of Technology) for his help in improving the performance of our code.

References

[1] Alfano G 2006 On the influence of the shape of the interface law on the application of cohesive-zone models *Compos. Sci. Technol.* **66** 723–30
[2] Arwade S R and Popat M 2009 Statistics and probabilistic modeling of simulated intergranular cracks *Probab. Eng. Mech.* **24** 117–27
[3] Babuška I, Caloz G and Osborn J E 1994 Special finite element methods for a class of second order elliptic problems with rough coefficients *SIAM J. Numer. Anal.* **31** 945–81
[4] Babuška I and Rheinboldt W C 1978 Error estimates for adaptive finite element computations *SIAM J. Numer. Anal.* **15** 736–54
[5] Carpinteri A and Colombo G 1989 Numerical analysis of catastrophic softening behaviour (snap-back instability) *Comput. Struct.* **31** 607–36
[6] Chen L, Ballarini R and Grigoriu M 2004 Crack propagation in a material with random toughness *Int. J. Fract.* **125** 353–69
[7] Corigliano A, Cacchione F, Frangi A and Zerbini S 2008 Numerical modelling of impact rupture in polysilicon microsystems *Comput. Mech.* **42** 251–9
[8] Curtin W A 1997 Toughening in disordered brittle materials *Phys. Rev.* B **55** 11270–6
[9] Duarte C A M and Oden J T 1996 An *hp* adaptive method using clouds *Comput. Methods Appl. Mech. Eng.* **139** 237–62
[10] Duarte C A, Reno L G and Simone A 2007 A high-order generalized FEM for through-the-thickness branched cracks *Int. J. Numer. Methods Eng.* **72** 325–51
[11] Duflot M and Bordas S 2008 *A posteriori* error estimation for extended finite elements by an extended global recovery *Int. J. Numer. Methods Eng.* **76** 1123–38
[12] Falk M L, Needleman A and Rice J R 2001 A critical evaluation of cohesive zone models of dynamic fracture *J. Phys.* IV **11** 43–50
[13] Grah M, Alzebdeh K, Sheng P Y, Vaudin M D, Bowman K J and Ostoja-Starzewski M 1996 Brittle intergranular failure in 2D microstructures: experiments and computer simulations *Acta Mater.* **44** 4003–18
[14] Gutiérrez M A 2004 Energy release control for numerical simulations of failure in quasi-brittle solids *Commun. Numer. Methods Eng.* **20** 19–29
[15] Harper P W and Hallett S R 2008 Cohesive zone length in numerical simulations of composite delamination *Eng. Fract. Mech.* **75** 4774–92
[16] Kraft R H and Molinari J F 2008 A statistical investigation of the effects of grain boundary properties on transgranular fracture *Acta Mater.* **56** 4739–49
[17] Luther T and Könke C 2009 Polycrystal models for the analysis of intergranular crack growth in metallic materials *Eng. Fract. Mech.* **76** 2332–43
[18] Maiti S, Rangaswamy K and Geubelle P H 2005 Mesoscale analysis of dynamic fragmentation of ceramics under tension *Acta Mater.* **53** 823–34
[19] Melenk J M and Babuška I 1996 The partition of unity finite element method: basic theory and applications *Comput. Methods Appl. Mech. Eng.* **139** 289–314
[20] Moës N and Belytschko T 2002 Extended finite element method for cohesive crack growth *Eng. Fract. Mech.* **69** 813–33
[21] Moës N, Dolbow J and Belytschko T 1999 A finite element method for crack growth without remeshing *Int. J. Numer. Methods Eng.* **46** 131–50

[22] Oden J T and Prudhomme S 2001 Goal-oriented error estimation and adaptivity for the finite element method *Comput. Math. Appl.* **41** 735–56
[23] Onck P and Van der Giessen E 1997 Influence of microstructural variations on steady state creep and facet stresses in 2-D freely sliding polycrystals *Int. J. Solids Struct.* **34** 703–26
[24] Onck P and Van der Giessen E 1997 Microstructurally-based modelling of intergranular creep fracture using grain elements *Mech. Mater.* **26** 109–26
[25] Rice R W, Freiman S W and Becher P F 1981 Grain-size dependence of fracture energy in ceramics: I. Experiment *J. Am. Ceram. Soc.* **64** 345–50
[26] Rice R W 1997 Ceramic tensile strength-grain size relations: grain sizes, slopes, and branch intersections *J. Mater. Sci.* **32** 1673–92
[27] Rivara M C 1989 Selective refinement/derefinement algorithms for sequences of nested triangulations *Int. J. Numer. Methods Eng.* **28** 2889–906
[28] Romero de la Osa M, Estevez R, Olagnon C, Chevalier J, Vignoud L, and Tallaron C 2009 Cohesive zone model and slow crack growth in ceramic polycrystals *Int. J. Fract.* **158** 157–67
[29] Sfantos G K and Aliabadi M H 2007 Multi-scale boundary element modelling of material degradation and fracture *Comput. Methods Appl. Mech. Eng.* **196** 1310–29
[30] Simone A, Duarte C A and Van der Giessen E 2006 A Generalized Finite Element Method for polycrystals with discontinuous grain boundaries *Int. J. Numer. Methods Eng.* **67** 1122–45
[31] Sukumar N, Srolovitz D J, Baker T J and Prévost J-H 2003 Brittle fracture in polycrystalline microstructures with the extended finite element method *Int. J. Numer. Methods Eng.* **56** 2015–37
[32] Turon A, Dávila C G, Camanho P P and Costa J 2007 An engineering solution for mesh size effects in the simulation of delamination using cohesive zone models *Eng. Fract. Mech.* **74** 1665–82
[33] Tvergaard V and Hutchinson J W 1992 The relation between crack growth resistance and fracture process parameters in elastic-plastic solids *J. Mech. Phys. Solids* **40** 1377–97
[34] van den Bosch M J, Schreurs P J G and Geers M G D 2006 An improved description of the exponential Xu and Needleman cohesive zone law for mixed-mode decohesion *Eng. Fract. Mech.* **73** 1220–34
[35] Van Siclen C D 2006 Intergranular fracture in model polycrystals with correlated distribution of low-angle grain boundaries *Phys. Rev.* B **73** 184118
[36] Verhoosel C V and Gutiérrez M A 2009 Modelling inter-and transgranular fracture in piezoelectric polycrystals *Eng. Fract. Mech.* **76** 742–60
[37] Waisman H and Belytschko T 2008 Parametric enrichment adaptivity by the extended finite element method *Int. J. Numer. Methods Eng.* **73** 1671–92
[38] Warner D H and Molinari J F 2006 Micromechanical finite element modeling of compressive fracture in confined alumina ceramic *Acta Mater.* **54** 5135–45
[39] Wei Y J and Anand L 2004 Grain-boundary sliding and separation in polycrystalline metals: application to nanocrystalline fcc metals *J. Mech. Phys. Solids* **52** 2587–616
[40] Xu X-P and Needleman A 1994 Numerical simulations of fast crack growth in brittle solids *J. Mech. Phys. Solids* **42** 1397–434
[41] Zavattieri P D, Raghuram P V and Espinosa H D 2001 A computational model of ceramic microstructures subjected to multi-axial dynamic loading *J. Mech. Phys. Solids* **49** 27–68
[42] Zienkiewicz O C and Zhu J Z 1987 A simple error estimator and adaptive procedure for practical engineering analysis *Int. J. Numer. Methods Eng.* **24** 337–57